Heliyon 8 (2022) e10683

Contents lists available at ScienceDirect

Heliyon

journal homepage: www.cell.com/heliyon

Research article

TiO_2-modified g-C_3N_4 nanocomposite for photocatalytic degradation of organic dyes in aqueous solution

Ntakadzeni Madima [a], Kebede K. Kefeni [a], Shivani B. Mishra [b,c], Ajay K. Mishra [b,c,d,*]

[a] Institute for Nanotechnology and Water Sustainability (iNanoWS), College of Science, Engineering and Technology, University of South Africa, Florida Science Campus, Florida, Roodepoort, Johannesburg, 1709, South Africa
[b] College of Pharmaceutical and Chemical Engineering, Hebei University of Science and Technology, Shijiazhuang, 050018, China
[c] Academy of Nanotechnology and Wastewater Innovations, Johannesburg, South Africa
[d] Department of Chemistry, Durban University of Technology, Steve Biko Road, 4001, Durban, South Africa

ARTICLE INFO

Keywords:
Green synthesis
Photocatalytic degradation
Nanocomposite
Radical scavenger

ABSTRACT

In the current study, a direct S-scheme titanium dioxide/graphitic carbon nitride (TiO_2/g-C_3N_4) heterojunction structure was fabricated via simultaneous calcination of TiO_2 precursors and g-C_3N_4. *Guava* leaf extract was utilized as a reductant for TiO_2 production through a green synthetic method, and g-C_3N_4 was prepared by thermal decomposition of melamine. The pristine and nanocomposite photocatalysts were characterized by XRD, FTIR, BET, TGA, HRTEM, UV–vis DRS, and PL to elucidate their physicochemical properties. The photocatalytic activity of synthesized photocatalysts was examined through the degradation of rhodamine B (RhB) and methylene blue (MB) dyes under simulated solar light irradiation. The nanocomposite exhibited commendable photocatalytic performances with 96% degradation efficiency of RhB attained in 120 min and 95% degradation efficiency of MB achieved in 150 min. The enhanced photocatalytic activities were attributable to visible light-harvesting characteristics and the formation of an S-scheme heterojunction system between two catalysts which promotes interfacial charge separation efficiency and longer charge carrier lifespan. After 4 consecutive cycles, the degradation efficiencies of both RhB and MB remained above 85%. According to the trapping experiments, $OH^{\bullet}$ and $O_2^{\bullet-}$ radicals were critical in the degradation of RhB, while h^+ and $O_2^{\bullet-}$ radicals were dominant in the degradation of MB. The nanocomposite was also tested for elution of actual water pollutants by combining two dyes, and above 90% degradation efficiencies were achieved for both dyes after 240 min.

1. Introduction

The existence of organic pollutants such as dye molecules in water systems has been a major concern across the globe due to the impact they impose on human activities and the ecosystem. Dye molecules such as methyl orange (MO), methylene blue (MB), rhodamine B (RhB), and others are extensively used in various industrial applications, ranging from food coloration, pH indicators, cosmetics, pharmaceuticals, textile coloration, and printing industries. A substantial amount of dye molecules is dissipated into water bodies during the dying process, posing a profound ultimatum to human health and the ecosystem due to their toxicity. Most dye molecules show mutagenic, carcinogenic, genotoxic, and teratogenic effects [1, 2, 3, 4, 5]. Consequently, it has become crucial to remove dye molecules from water sources.

Amongst different methods used for the remediation of dye molecules in water, photocatalysis has emerged as a promising option for removing a wide range of dye molecules due to its capacity to completely mineralize dye molecules into unharmful substances like water and carbon dioxide [6, 7]. Photocatalysis utilizes sunlight in the presence of semiconductor nanomaterials to photodegrade complex organic dye structures into unharmful substances. Different semiconductor nanomaterials have been utilized and among them, titanium dioxide (TiO_2) has sparked a lot of interest due to its distinctive qualities including non-toxicity, high chemical stability, strong oxidizing power, reactive surface, and low production cost [8, 9, 10].

Nevertheless, although TiO_2 has been at the forefront of photocatalysis, its practical application is still hindered by drawbacks such as large energy bandgap (~3.2 eV) and fast recombination rate of photoinduced charge carriers. The wide energy bandgap of TiO_2

* Corresponding author.
E-mail address: ajaykmisharedu@gmail.com (A.K. Mishra).

https://doi.org/10.1016/j.heliyon.2022.e10683
Received 10 March 2022; Received in revised form 14 June 2022; Accepted 13 September 2022

makes it photoactive in the ultraviolet region which only accounts for a low portion of the solar light spectrum [11]. Considering this, it is of greater interest to reduce the energy bandgap of TiO_2 to utilize a large fragment of the solar light spectrum that is available in excess, which is the visible region. Additionally, the faster recombination rate of charge carriers has been the bigger obstacle to completely utilizing TiO_2 in photocatalysis, since it results in poor photocatalytic efficiency [12].

Therefore, enhancing the photocatalytic effectiveness of TiO_2 has been the focus of extensive research. These focuses comprise doping TiO_2 with either metal or non-metal and coupling TiO_2 with other semiconductor nanomaterials. Doping results in the formation of defects states within the band levels of TiO_2 that in turn reduces the energy needed to excite electrons from the valence band to the conduction band, while coupling TiO_2 with other semiconductors nanomaterials results in the enhancement of electron-hole pair charge separation through the transfer of electrons and holes between the semiconductor nanomaterials [13, 14, 15].

Recently, the coupling of TiO_2 with graphitic carbon nitride (g-C_3N_4) has received significant interest owing to their well-matched band position levels [16, 17, 18]. Graphitic carbon nitride is also one of the semiconductor materials which has received much interest in photocatalysis in the last decade due to its medium energy bandgap (~2.7 eV), nontoxicity, and low production cost [8, 19, 20, 21]. Its application in photocatalysis is hindered by its poor energy band gap, rapid recombination of electron-hole pairs, and small surface area. So, the modification of g-C_3N_4 is as significant as those for TiO_2. Therefore, most researchers have proved that the coupling of g-C_3N_4 with TiO_2 is of greater importance benefiting from both g-C_3N_4 and TiO_2 properties [22, 23, 24, 25, 26, 27]. The coupling of those two semiconductor materials has been at the forefront of many researchers, due to the improved properties of individuals that result in higher photocatalytic activities and efficiency [23, 25, 28].

In the last decade, numerous methods have been broadly used to synthesize nanomaterials. However, to control their size and shape, most of the chemical and physical methods need the inclusion of certain chemicals in the form of inhibitors and reducing agents. Most of the stabilizers are hazardous chemicals that compromise the application of synthesized nanomaterials in water purification. Recently, green synthesis methods using plant extracts as reducing and stabilizing agents have received a lot of interest because of their eco-friendly, safe, and low-cost properties [14, 29, 30, 31, 32, 33, 34, 35, 36, 37]. Amongst various plants, *Guava* leaves have been widely used in the synthesis of nanomaterials for various applications owing to their medical properties and abundance. They are commonly found in various parts of the countries within tropical and subtropical regions. Their extracts contain a large number of phytochemicals such as flavonoids, tannins, and phenolic acids, which can act as inhibitors or capping agents to regulate the formation of crystals and the morphology of nanomaterials [32, 33, 38, 39].

In the previous work of our group, we demonstrated the photocatalytic degradation of RhB over magnetic Fe_3O_4/TiO_2 heterostructure photocatalyst [40]. We investigated the influence of several factors on the photocatalytic performance of the photocatalysts. In connection with our previous work, the current study report on a novel and facile method for the development of an S-scheme heterojunction photocatalyst between green synthesized TiO_2 nanoparticles and pristine g-C_3N_4 for the photocatalytic degradation of RhB and MB dye contaminants. Pristine g-C_3N_4 was prepared through the thermal polymerization of melamine, and a direct S-scheme TiO_2/g-C_3N_4 heterojunction photocatalyst was obtained through simple one-port calcination of green TiO_2 precursors and pre-synthesized g-C_3N_4.

2. Experimental setup

2.1. Chemicals

Titanium (IV) tetraisopropoxide (TTIP) (98%), Melamine, Absolute ethanol, Formic acid (FA), Isopropanol (ISP), Ascorbic acid (AA), Rhodamine B (RhB), and Methylene blue (MB) were purchased from Sigma Aldrich and employed without further purifying.

2.2. Guava leaves extraction

Guava leaves extraction was done by the method described in our previous work [40].

2.3. Synthesis of anatase TiO_2 and pristine g-C_3N_4

Green synthesis of TiO_2: The synthesis procedure was similar to our previous work with minor modifications [40]: TTIP (5 mL) was added to 20 mL H_2O, which was then followed by the addition of 5 ml *Guava* leaf extracts. The mixture was magnetically stirred at 60 °C for 2 h. Then the yellow precipitate was obtained and left to dry. Eventually, the dried resultant was annealed at 350 °C for a period of 5 h at the ramping rate of 5 °C/min.

Preparation of pristine g-C_3N_4: pristine g-C_3N_4 was prepared through thermal decomposition of melamine [41, 42]. Briefly, 1 g of melamine was put in a ceramic crucible and heated at 520 °C for 3 h in a muffle furnace with a ramping rate of 5 °C/min under an air atmosphere. The pristine g-C_3N_4 was collected and grind into fine powder after cooling the muffle furnace to room temperature.

2.4. Preparation of TiO_2/g-C_3N_4 nanocomposite

The as-synthesized g-C_3N_4 was dispersed in 50 mL ethanol under sonication for 1 h, while on the other hand, the mixture of TTIP and *Guava* leaf extracts was stirred at 60 °C for 2 h. Then, the mixture containing TTIP, and leaf extracts was added to the suspension of g-C_3N_4, and the mixture was stirred for a further 1 h at 60 °C. Afterward, the mixture was allowed to cool and washed multiple times, then dried at 60 °C. Finally, the prepared TiO_2/g-C_3N_4 nanocomposite was added into a crucible and heated in a muffle furnace at 520 °C for 5 h at the ramping rate of 5 °C/min. The graphical demonstration of the synthesis setup of TiO_2/g-C_3N_4 nanocomposite is displayed in Scheme 1.

2.5. Photocatalytic activity evaluation

The photocatalytic activity of synthesized photocatalysts was appraised by the degradation of RhB and MB as the modern dye's pollutants. In a typically photocatalytic reaction, 50 mg of photocatalysts and 100 mL containing 10 mg L^{-1} dye concentration were utilized in both experiments. The solution was irradiated with an Asahi HAL-320 Solar Simulator fitted with a 300 W compact xenon lamp that produced visible light intensity of 100 mW cm^{-2}. The solar simulator was warmed up for 60 min before irradiation. Prior to light irradiation, the solution containing a suspended photocatalyst and dye solution was agitated for 30 min in the dark to equilibrate the catalyst and dye. Then, the solution was submitted to solar light irradiation while being constantly agitated by a magnetic stirrer. At regular time intervals (20 min for RhB and 30 min for MB), 2 mL aliquots were withdrawn and filtered with a microspore syringe filter (0.45 μm), and the filtrates were analyzed using a UV-vis spectrophotometer. The percentage removal was estimated using Eq. (1):

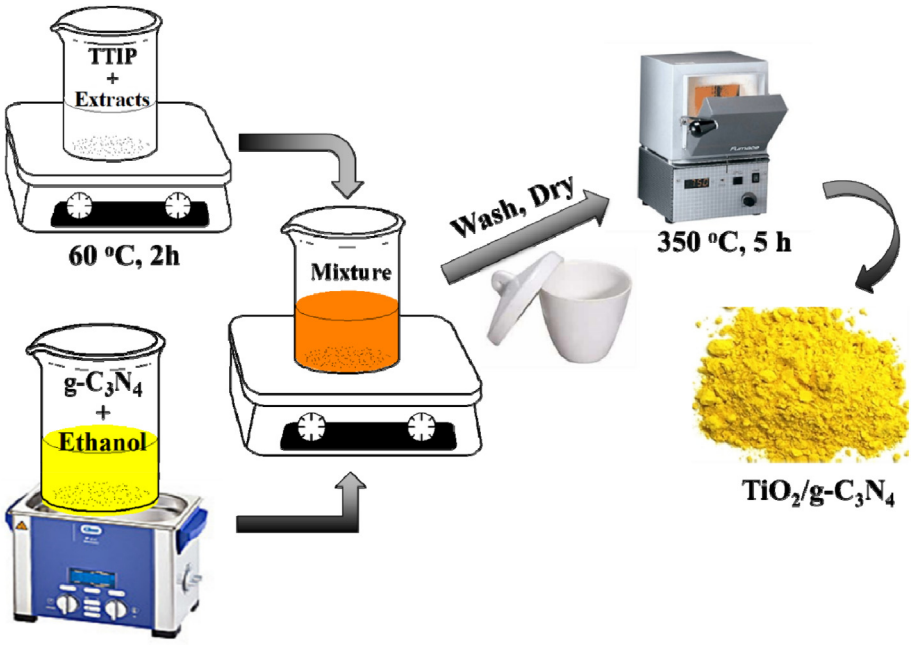

Scheme 1. Schematic presentation of the synthesis set-up of TiO_2/g-C_3N_4 nanocomposite.

$$\textit{Percentage removal} = \left(1 - \frac{A_t}{A_o}\right) \times 100 \quad (1)$$

where: A_t and A_o are the real-time and initial absorbance of dye solution, respectively. To determine the photocatalyst stability, the catalyst was recovered and subsequently used once more in the same experiment after each reaction. The catalyst was collected through filtration and washed multiple times with H_2O and absolute ethanol to eliminate dye impurities that were adhered to the catalyst's surface, then dried and reused.

2.6. Characterization techniques

The X-ray diffraction (XRD) analysis of prepared photocatalysts was studied in a Rigaku Ultima IV X-ray diffractometer with Cu-Kα radiation (λ = 0.15406 nm) at the 2θ range of 10–70°. The Fourier transform infrared (FT-IR) spectra of the as-synthesized photocatalysts were recorded using a PerkinElmer FT-IR spectrometer utilizing the KBr pellet technique. The thermal stability of prepared photocatalysts was examined using TGA 5500 Discovery series (TA instruments) from room temperature to 900 °C. The form of the porous structures and specific surface area were studied on an Autosorb iQ3 provided by Anton Par equipped with a vacuum degassing pump. High-resolution transmission electron microscopy (HRTEM) images and the selected area electron diffraction (SAED) pattern were recorded using a JEOL-JEM-2100 (JOEL, Japan). The UV–vis analysis was recorded on PerkinElmer UV–vis spectrometer Lambda 650. Photoluminescence spectra were analyzed on Horiba Fluorlog 3 FL3, xenon lamp.

3. Results and discussion

3.1. Characterization

3.1.1. XRD analysis

The crystallographic structure of synthesized photocatalysts was examined using XRD and experimental data are displayed in Figure 1. Pristine g-C_3N_4 (Figure 1a) displays two typical diffraction peaks at 2-θ position 15.5° corresponding to the (100) plane of tri-s-triazine units of g-C_3N_4 and another at peak 29.9° corresponding to (002) plane of interlayer stacking of conjugated aromatic system of g-C_3N_4 (JCPDS Card No. 87-1526) [25, 43]. Green synthesized TiO_2 (Figure 1c) shows

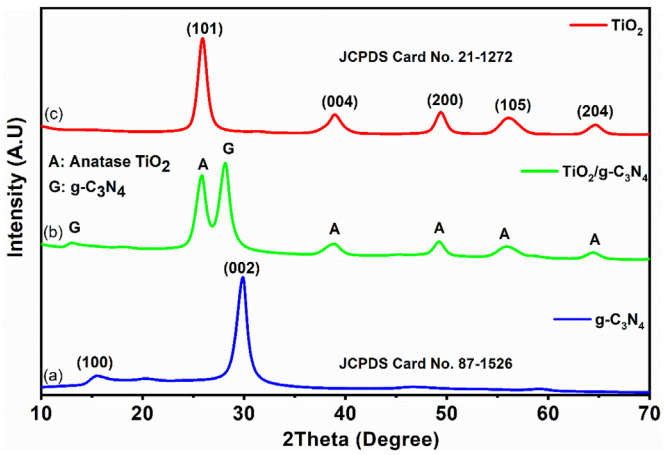

Figure 1. XRD spectra of synthesized (a) g-C_3N_4, (b) TiO_2/g-C_3N_4 nanocomposite, and (c) TiO_2.

the diffraction peaks corresponding to anatase phase TiO_2 (JCPDS Card No. 21-1272) [11, 40]. The XRD pattern for the TiO_2/g-C_3N_4 nanocomposite (Figure 1b) reveals diffraction peaks of both green synthesized TiO_2 and pristine g-C_3N4, which indicate the coexistence of these compounds in the nanocomposite. The diffraction peak of g-C_3N_4 slightly shifted to lower 2-θ angles when coupled with TiO_2, demonstrating a strong relation between g-C_3N_4 and TiO_2. The average crystalline size (Dp) of synthesized samples was estimated from the XRD data via Scherrer's equation as represented by Eq. (2):

$$Dp = \frac{\kappa\lambda}{\beta cos\theta} \quad (2)$$

where $\boldsymbol{k}$, λ, $\boldsymbol{\beta}$, and $\boldsymbol{\theta}$ are the constant (0.94), the wavelength of X-ray (0.15406 nm), the peak full width half maximum (FWHM), and the angle of reflection, respectively. The estimated average crystalline sizes were 6.30 nm, 5.64 nm, and 6.68 nm for TiO_2, g-C_3N_4, and TiO_2/g-C_3N_4 nanocomposite, respectively.

3.1.2. FTIR spectroscopy and TGA analysis

To further confirm the surface structural properties of synthesized photocatalysts, FTIR analysis was conducted, and the results are displayed in Figure 2. The FTIR spectrum of g-C_3N_4 (Figure 2a), shows strong characteristics peaks at the frequency range of 1700–1200 cm^{-1} which were accredited to the typical stretching mode of C–N heterocycles of g-C_3N_4 [11]. The strong intense peak observed near 810 cm^{-1} was assigned to the out-of-plane bending vibration mode of triazine units [27]. The broad absorption band around 3700–3000 cm^{-1} can be attributed to the OH stretching vibration corresponding to the adsorbed H_2O on the surface of g-C_3N_4 and NH_2 or NH groups at the defect sites of the aromatic ring [44, 45]. The spectrum of TiO_2 (Figure 2c) displays a broad band at around 800–400 cm^{-1} which is assigned to the Ti–O–Ti and Ti–O stretching vibration modes in anatase crystals [40, 44]. The absorption bands observed around 3400 cm^{-1} and 1636 cm^{-1} were ascribed to the bending and stretching vibration of surface adsorbed OH groups and H_2O, respectively. As evident from the spectrum of TiO_2/g-C_3N_4 nanocomposite (Figure 2b), all the typical peaks of both compounds are observed as expected, confirming an effective coupling of TiO_2 with g-C_3N_4.

The thermal stability of the as-prepared photocatalysts was studied using gravimetric analysis and the results are displayed in Figure 3. The TGA spectrum of g-C_3N_4 (Figure 3a) shows a substantial weight reduction at 580–700 °C due to the decay of g-C_3N_4 to form CO_2 and graphite [11, 44]. The spectrum of TiO_2/g-C_3N_4 nanocomposite (Figure 3b) shows a rapid weight loss in the range of 500–600 °C, which can be accredited to the decomposition of g-C_3N_4. The retained weight loss in the nanocomposite spectrum is due to TiO_2 weight. The decay of g-C_3N_4 occurs at a lower temperature in nanocomposite as compared to that of pristine g-C_3N_4 which is due to the distribution of TiO_2 nanoparticles onto the surface of g-C_3N_4 which results in weakening the van der Waals forces between g-C_3N_4 layers [43]. The TGA spectrum of TiO_2 (Figure 3c) shows no significant weight loss indicating higher thermal stability properties of TiO_2 nanoparticles. In addition, both spectra show a smaller weight loss at the temperature region of 0–250 °C, which can be accredited to the evaporation of water molecules adsorbed on the surface of the catalysts.

3.1.3. BET analysis

Nitrogen adsorption-desorption analysis were carried out to determine the nature of the porous structures and the surface area of the produced photocatalysts and the results are shown in Figure 4a. All synthesized photocatalysts resemble type IV isotherms according to the IUPAC description [16, 17], which implies that all samples possess mesoporous structures (2–50 nm). The isotherms of TiO_2 nanoparticles had an H2-type hysteresis loop indicating ink-bottle pore structure, while

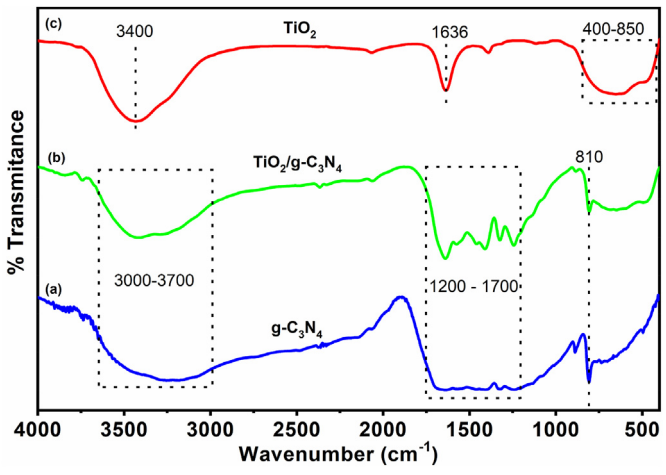

Figure 2. The FTIR spectra of synthesized samples (a) g-C_3N_4, (b) TiO_2/g-C_3N_4 nanocomposite, and (c) TiO_2.

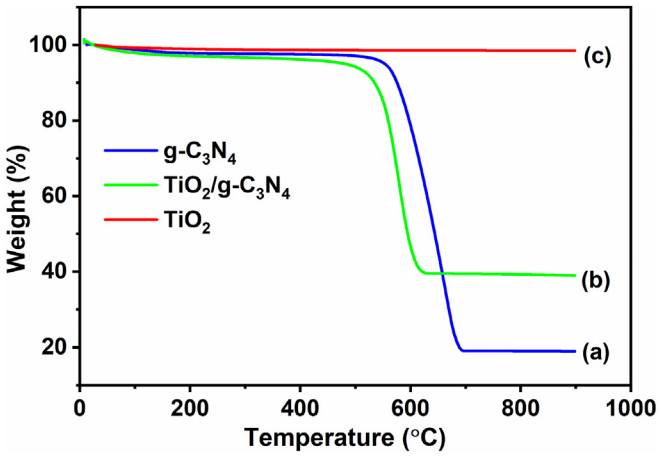

Figure 3. TGA curves of (a) g-C_3N_4, (b) TiO_2/g-C_3N_4 nanocomposite, and (c) TiO_2.

the isotherms of g-C_3N_4 and the nanocomposite had an H3-type hysteresis loop designating the emergence of slit-like pore structure [46]. Table 1 demonstrates the measured surface areas, total pore volumes, and average pore radius of the synthesized photocatalysts.

The highest surface area is observed for TiO_2 nanoparticles in comparison with pristine g-C_3N_4 and TiO_2/g-C_3N_4 nanocomposite. Upon coupling, the surface area of TiO_2 decreases drastically, owing to the blocking of surface-active sites of TiO_2 by g-C_3N_4 [44]. The surface area of TiO_2/g-C_3N_4 nanocomposite is observed to be superior to g-C_3N_4. Furthermore, the pore size distribution was also measured by Barrett-Joyner-Halenda (BJH) method as shown in Figure 4b. The results show that the pore size distributions of synthesized photocatalysts are predominantly between 2 and 30 nm, and that is the characteristic feature of a mesoporous configuration. A higher surface area enhances the adsorption capability because of the presence of more active sites, while a larger pore structure allows for more dye contaminants to be adsorbed on the surface of the photocatalysts.

3.1.4. UV-vis analysis

Figure 5 illustrates the UV–visible diffuse reflectance spectra (DRS) of synthesized photocatalysts. As illustrated in Figure 5a: TiO_2 nanoparticles exhibit robust ultraviolet (UV) light absorption with an absorption edge at 388 nm. Pristine g-C_3N_4 shows intensive light absorption capability in both ultraviolet and visible light regions with an absorption edge at 459 nm. The light absorption of pristine g-C_3N_4 in the ultraviolet is lower than that of TiO_2 and these results are compatible with the previous work conducted by Wang *et.al* [41]. Meanwhile, upon coupling TiO_2 with g-C_3N_4, the nanocomposite exhibits a little improvement in visible light absorption as equated to TiO_2 owing to the strong and wide absorption band of g-C_3N_4 in the visible region. The absorption edge of the nanocomposite is around 400 nm which shows a red shift as compared to pure TiO_2, which can be credited to the interaction between g-C_3N_4 and TiO_2. The enhancement of light absorption of the nanocomposite in both ultraviolet and visible regions is crucial for photocatalytic activity under solar light irradiation. Further, the energy band gaps of synthesized photocatalysts were measured using the Tauc plot according to Eq. (3) [47]:

$$(\alpha h\nu)^2 = A(h\nu - E_g) \tag{3}$$

where α is the absorption coefficients, h is Planck's constant, υ is the light frequency, E_g is the energy band gap, and A is a constant. The estimated energy bandgaps ((Figure 5b).) for TiO_2, g-C_3N_4, and TiO_2/g-C_3N_4 nanocomposite were 3.2 eV, 2.7 eV, and 3.1 eV, respectively. The decrease in the energy band gap of TiO_2 upon coupling was attributed to

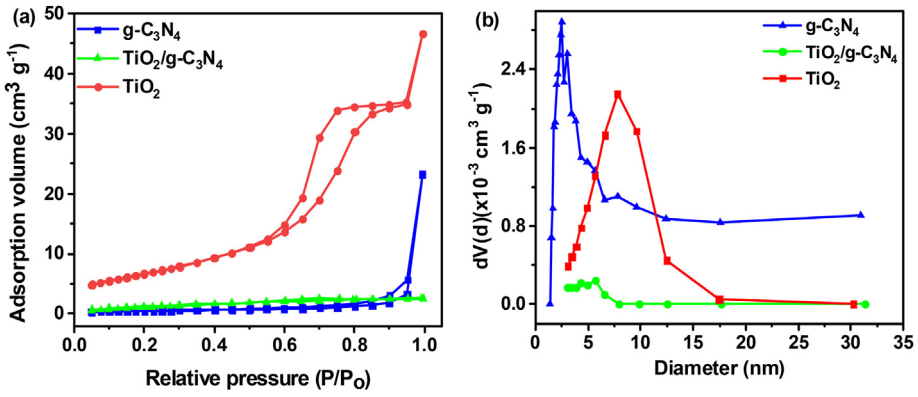

Figure 4. (a) N_2 adsorption-desorption isotherm and (b) Pore size distribution of g-C_3N_4, TiO_2/g-C_3N_4 nanocomposite, and TiO_2.

Table 1. BET analysis results of g-C_3N_4, TiO_2/g-C_3N_4 nanocomposite, and TiO_2.

Photocatalysts	Surface area ($m^2\ g^{-1}$)	Total pore volume ($cm^3\ g^{-1}$)	Average pore radius (nm)
g-C_3N_4	10.41	0.23	8.66
TiO_2	162.76	1.47	19.47
TiO_2/g-C_3N_4	32.53	0.03	2.60

the addition of the g-C_3N_4 phase, which stimulates the generation of more charge carriers in the nanocomposite under visible light radiation.

3.1.5. Photoluminescence (PL) analysis

To examine the rate of recombination of charge carriers in the synthesized photocatalysts, photoluminescence (PL) analysis was conducted at the excitation wavelength of 340 nm. Higher emission intensity in PL spectra indicates a high recombination probability [48]. Figure 6 exhibits the PL emission spectra of pristine g-C_3N_4, TiO_2/g-C_3N_4 nanocomposite, and pure TiO_2. The PL spectrum of g-C_3N_4 exhibits a strong photoluminescence signal, demonstrating a high recombination rate of electron-hole pair. The main emission peak of g-C_3N_4 is at about 455 nm, which is accredited to the band-band PL sensation, with the photon energy roughly equivalent to the g-C_3N_4 energy band gap (2.7 eV). The band-band PL signal arises from excitonic PL caused by n→𝛑 electronic transitions due to the lone pairs of nitrogen atoms in g-C_3N_4 [41]. The PL spectra of TiO_2 nanoparticles and TiO_2/g-C_3N_4 nanocomposite show a lower photoluminescence signal indicating a low recombination rate of electron-hole pairs which is beneficial in photocatalysis. In comparison, TiO_2/g-C_3N_4 nanocomposite shows a higher recombination rate of electron-hole pairs and broader luminescence peak than TiO_2, as a result of g-C_3N_4 visible light absorption capability.

3.1.6. HRTEM analysis

The morphological structure of synthesized TiO_2/g-C_3N_4 nanocomposite was explored by HRTEM, and the results are displayed in Figure 7. As evident from Figure 7a, pristine g-C_3N_4 has a transparent 2D nano sheet-like structure, while TiO_2 appears as spherical nanoparticles. On the other hand, since the nanoparticles show a well-defined morphology, the average grain size was estimated to be 14.4 nm (Figure 7b). The lattice fringe of TiO_2 in the nanocomposite was measured to be 0.348 nm (Figure 7c). The measured lattice fringe of TiO_2 correspond to the (101) plane of anatase TiO_2, and the pristine g-C_3N_4 shows no clear lattice fringes [49]. These findings show that TiO_2 binds closely to g-C_3N_4 to form a heterojunction structure that is advantageous for improving charge separation and photocatalytic activity [50]. The SAED pattern (Figure 7d), confirms the crystalline nature as well as the purity of the nanocomposite.

3.2. Photocatalytic activity measurements

3.2.1. Photodegradation of RhB and MB dye molecules

The photocatalytic performance of synthesized photocatalysts was observed by monitoring the main absorption peak of RhB and MB at 553 nm and 664 nm, respectively. Figure 8(a and b) show the UV-vis spectra

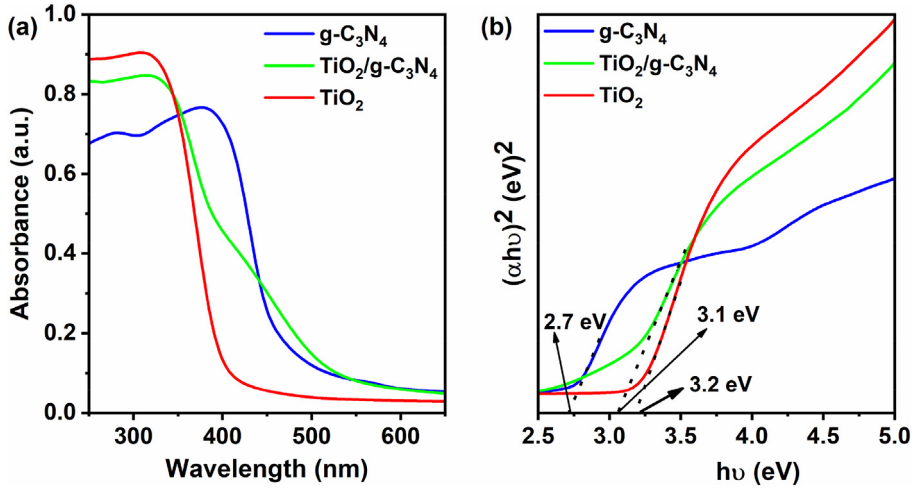

Figure 5. (a) UV-vis spectra of g-C_3N_4, TiO_2/g-C_3N_4 nanocomposite, and TiO_2, and (b) the bandgap estimation of g-C_3N_4, TiO_2/g-C_3N_4 nanocomposite, and TiO_2 determined from Tauc plot.

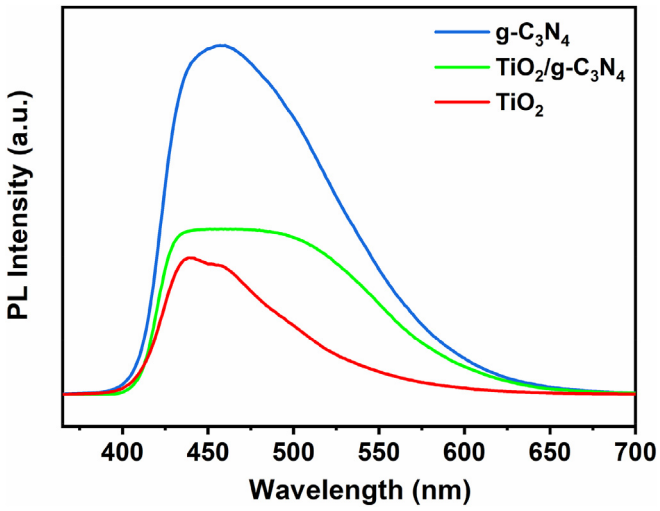

Figure 6. Photoluminescence spectra of g-C_3N_4, TiO_2/g-C_3N_4 nanocomposite, and TiO_2.

of RhB and MB over TiO_2/g-C_3N_4 nanocomposite and it can be seen that the maximum absorbance peak of RhB and MB decreases with an increase in irradiation time. The comparison of the photodegradation rates is given in Figure 8(c and d) together with the adsorption and photolysis study experiments. The photolysis study reveals that both RhB and MB degradation are photocatalyst-assisted processes since only a slight removal of RhB and MB was observed in the absence of a photocatalyst. The adsorption study experiments were carried out for TiO_2/g-C_3N_4 nanocomposite and the results reveal that the degradation of RhB and MB is a light-supported system, since only 30% (RhB) and 29% (MB) removal efficiency were attained after 120 min and 150 min, respectively. The degradation efficiencies of RhB and MB over nanocomposite were obtained to be 96% (120 min) and 95% (150 min), respectively, calculated using Eq. (1). In the comparison, TiO_2/g-C_3N_4 nanocomposite show higher degradation efficiency of RhB, and MB as compared to pure TiO_2 and pristine g-C_3N_4. The improved photocatalytic activity of the nanocomposite can be credited to the enhancement in photogenerated charge separation due to the development of the S-scheme heterojunction structure.

Figure 8(e and f) illustrate the linear pseudo-first-order kinetic reaction of RhB and MB, respectively. The photocatalytic degradation reaction rate constants for RhB are 0.02448, 0.00657, and 0.00601 min^{-1}, while for MB are 0.01718, 0.00680, and 0.00421 min^{-1} for TiO_2/g-C_3N_4, TiO_2, and g-C_3N_4, respectively. The nanocomposite rate constants for RhB are 3.7 and 4.1 folds higher than TiO_2 and g-C_3N_4; and 2.5 and 4.1 folds more than TiO_2 and g-C_3N_4 for MB degradation, respectively. Table 2 lists the apparent rate constants of the developed photocatalysts as well as a summary of photodegradation efficiencies.

3.2.2. *Re-usability study*

The re-usability study was also conducted to examine the stability of synthesized nanocomposite during photocatalysis. After each reaction, the nanocomposite was recycled and employed in a subsequent experiment. As illustrated in Figure 9(a and b), the photocatalytic degradation efficiency of RhB decreases from 96% to 88% (Figure 9a), while the degradation efficiency of MB decreases from 95% to 87% (Figure 9b) after four cycles. Furthermore, the XRD pattern, and FTIR spectra of the nanocomposite after four degradation cycles of MB was compared to that of the fresh nanocomposite. No phase change was observed in the XRD pattern (Figure 9(c)) of TiO_2/g-C_3N_4 nanocomposite after 4 cycles demonstrating good stability of the nanocomposite. The FTIR spectrum of nanocomposite after four degradation cycles (Figure 9(d)) shows an additional functional group around 1646 cm^{-1} due to the C=N stretching vibration of adsorbed MB in the nanocomposite [51, 52]. Therefore, a slight reduction in degradation effectiveness after four cycles can be associated with the loss of surface-active sites of the catalyst as a result of the pollutants' adsorption, which prevents proper light absorption. The degradation efficiencies after four cycles remained above 85% of their initial value, demonstrating the nanocomposite's high level of stability.

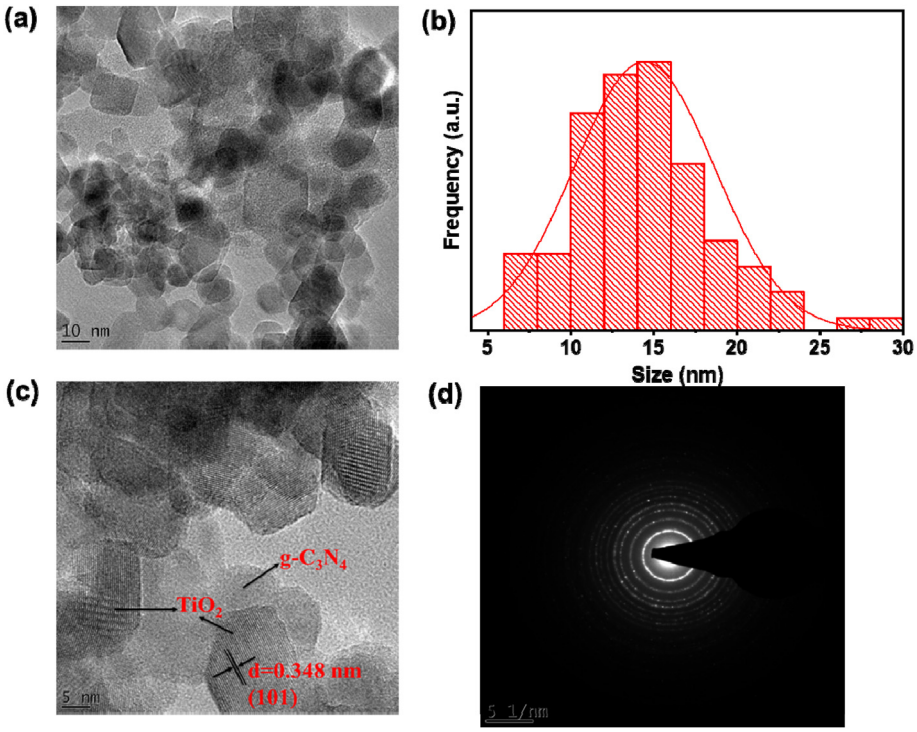

Figure 7. (a) TEM image, (b) the grain size distribution, (c) HRTEM image, and (d) SAED pattern of TiO_2/g-C_3N_4 nanocomposite.

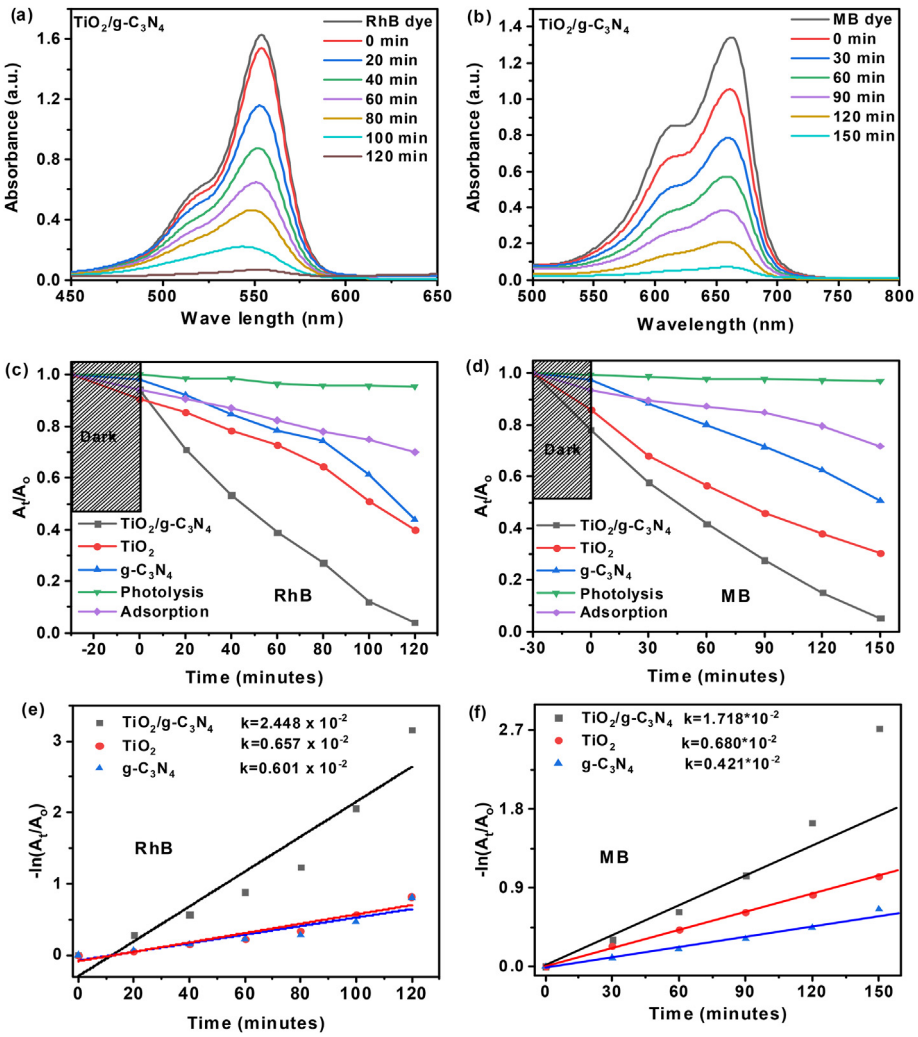

Figure 8. UV-vis absorbance spectra of (a) RhB, (b) MB, the photocatalytic degradation rate of (c) RhB, (d) MB, and the pseudo-first-order kinetic plots of (e) RhB, and (f) MB, over synthesized photocatalysts.

Table 2. Summary of photocatalytic degradation activities of RhB and MB: degradation efficiency, and apparent rate constant (k_{app}) over synthesized photocatalysts.

Photocatalysts	RhB		MB	
	Degradation efficiency (%)	K_{app} (x10^{-2} min^{-1})	Degradation efficiency (%)	K_{app} (x10^{-2} min^{-1})
TiO_2/g-C_3N_4	96	2.448	95	1.718
TiO_2	60	0.657	70	0.680
g-C_3N_4	56	0.601	50	0.421

3.2.3. Radical scavengers test

To distinguish which reactive oxygen species (ROS) plays the major role in the photodegradation process of RhB and MB dyes over the synthesized TiO_2/g-C_3N_4 nanocomposite different quenchers of ISP, AA, and FA were employed to trap the hydroxyl radical ($OH^{\bullet}$), superoxide radicals ($O_2^{\bullet-}$) and hole (h^+), respectively and results are displayed in Figure 10. For photodegradation of RhB (Figure 10a), the introduction of FA shows no significant reduction in photocatalytic performance indicating that h^+ is not the dominant ROS; while adding AA and ISP shows a drastic decline in photodegradation efficiency indicating that both $OH^{\bullet}$ and $O_2^{\bullet-}$ radicals are primarily ROS responsible for the degradation of RhB dye. Meanwhile, for the photodegradation of MB (Figure 10b), the addition of ISP did not affect the photodegradation efficiency of the nanocomposite which indicates that $OH^{\bullet}$ radicals did not play an astounding role in the degradation of MB. The addition of FA and AA results in a significant decrease in photocatalytic activity of the nanocomposite, indicating that both $O_2^{\bullet-}$ radicals and h^+ are two key ROS dominating degradation of MB dye.

3.2.4. Proposed photocatalytic degradation mechanism

To understand the mechanism behind the photocatalytic degradation of RhB and MB the results of the radical scavenger test were used. Firstly, the conduction band (CB) and valence band (VB) potentials of TiO_2 and g-C_3N_4 were obtained using Eqs. (4) and (5), respectively [53]:

$$E_{CB} = X - E_C - 0.5E_G \quad (4)$$

$$E_{VB} = E_{CB} + E_G \quad (5)$$

where X, E_C, E_g, E_{CB}, and E_{VB} are the absolute electronegativity of semiconductors (X for g-C_3N_4 ~ 4.72 and TiO_2 ~ 5.81), the energy of free electrons on the hydrogen scale (~4.5 eV), the energy band gap of the photocatalyst, CB potential and VB potential, respectively. The estimated CB and VB potentials for TiO_2 and g-C_3N_4 are −0.3 eV and 2.9 eV, −1.1 eV and 1.6 eV, respectively. The CB potential of TiO_2 (−0.29 eV) is less than the potential of $O_2/O_2^{\bullet-}$ (−0.33 eV vs. NHE), so the CB photogenerated electrons of TiO_2 cannot reduce dissolved oxygen and yield

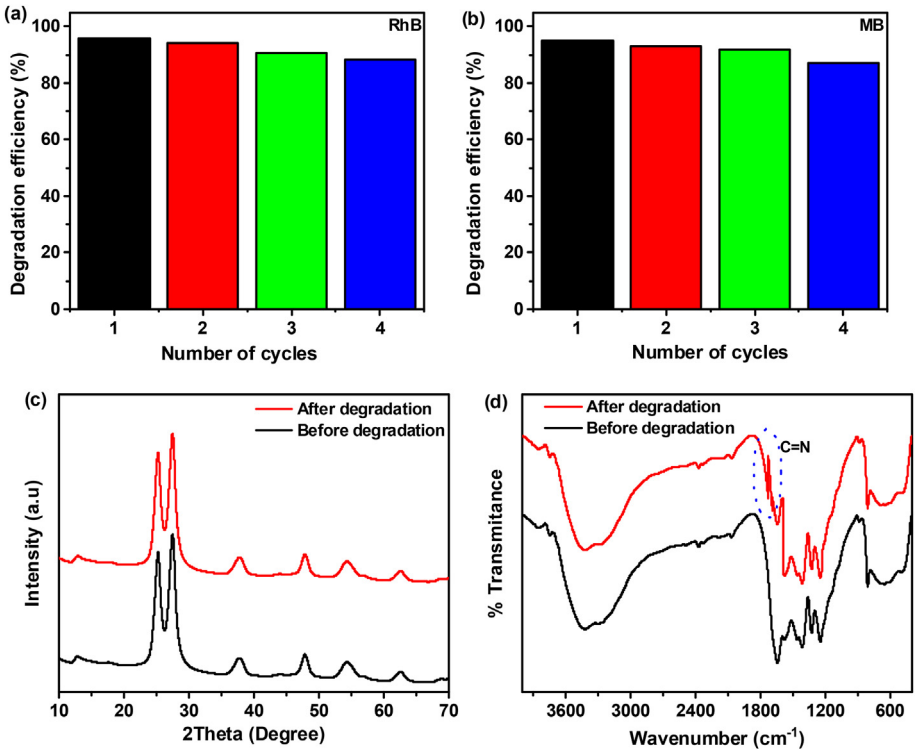

Figure 9. (a and b) reusability study, (c) X-ray diffraction patterns, (d) FTIR spectrum, of TiO_2/g-C_3N_4 nanocomposite before and after 4 circulating runs.

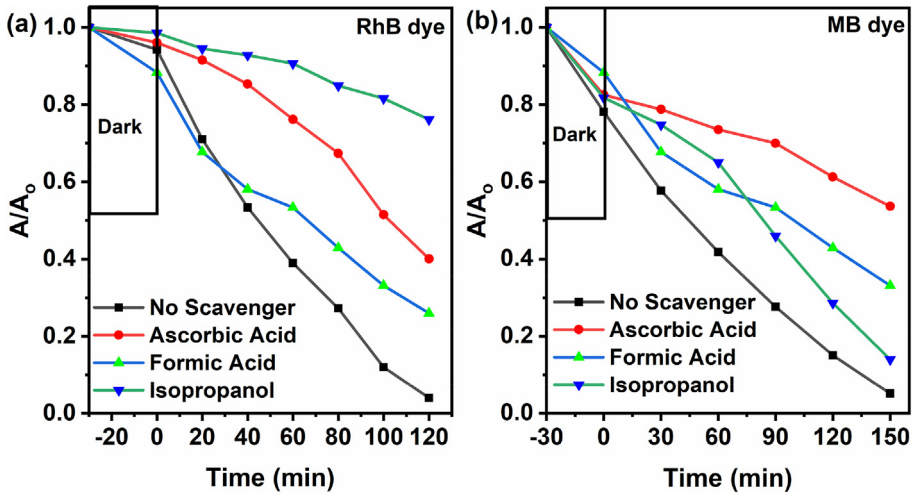

Figure 10. Photodegradation efficiency of (a) RhB, and (b) MB, over TiO_2/g-C_3N_4 nanocomposite with different scavengers.

$O_2^{\bullet-}$ radicals, whereas the CB potential of g-C_3N_4 (−1.1 eV) is more negative than the potential of $O_2/O_2^{\bullet-}$ (−0.33 eV vs. NHE), and thus the photoinduced electrons on the CB of g-C_3N_4 can reduce O_2 to $O_2^{\bullet-}$ radicals. Meanwhile, the redox potential of $OH^{\bullet}/H_2O$ (2.68 eV vs. NHE) is less positive than the VB potential of TiO_2 (2.9 eV) so the VB holes of TiO_2 can oxidize the water molecules to form $OH^{\bullet}$ radicals, while the holes in VB of g-C_3N_4 cannot oxidize adsorbed H_2O molecules to form $OH^{\bullet}$ radicals due to its VB potential being more negative than the potential of $OH^{\bullet}/H_2O$ (2.68 eV vs. NHE) [54]. Based on the above findings, an S-scheme heterojunction photocatalytic mechanism can be constructed as depicted in Scheme 2, which is in line with the findings of the aforementioned quenching experiment.

Therefore, when exposed to solar light, TiO_2 and g-C_3N_4 simultaneously absorbed photon energy. As a result, electrons are driven from the VB to the CB and leave positively charged holes in the VB, creating electron-hole pairs. The photogenerated electrons in g-C_3N_4 get donated to an electron acceptor such as dissolved O_2 resulting in the production of $O_2^{\bullet-}$ radicals which then degrade MB and RhB dye molecules. Since the

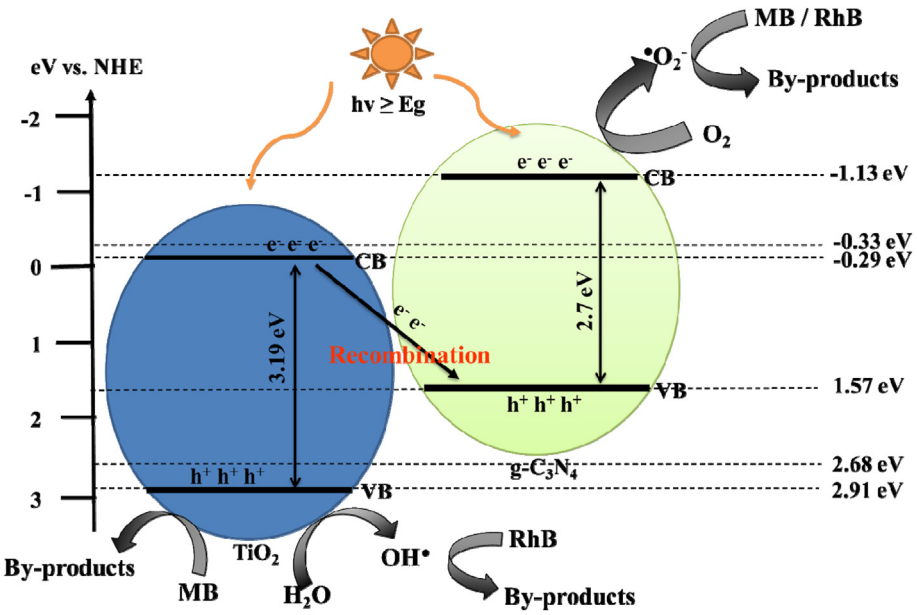

Scheme 2. S-schematic diagram of photogenerated charge transfer between TiO_2 and g-C_3N_4.

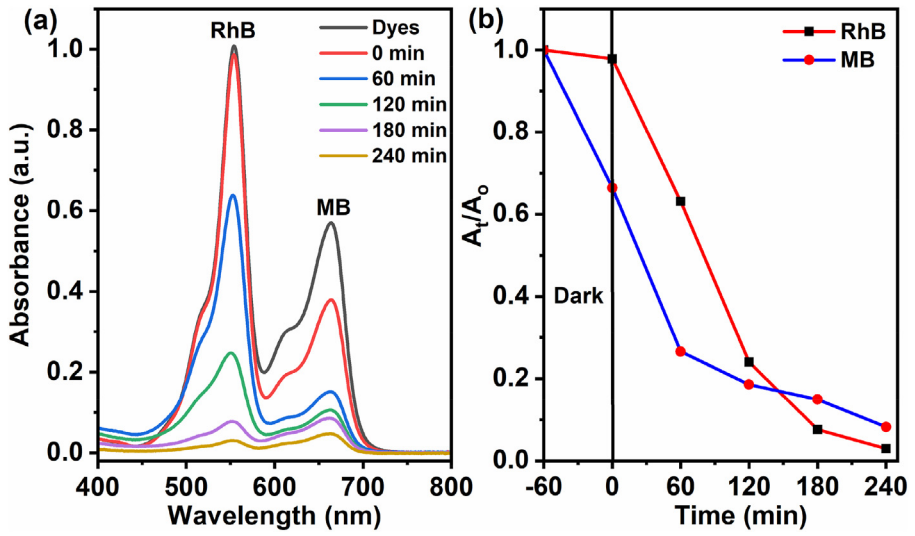

Figure 11. (a) UV-vis absorption spectrum of co-dyes photocatalytic degradation, and (b) photocatalytic degradation of RhB and MB for various irradiation times.

photogenerated electrons in the CB of TiO_2 cannot reduce O_2 to $O_2^{\bullet-}$ radicals, they recombine with the VB holes of g-C_3N_4. The transfer of electrons of TiO_2 to the VB of g-C_3N_4 reduced the rate of electron and hole recombination in TiO_2, which subsequently increased the photocatalytic activity of the nanocomposite. Additionally, the recombination of TiO_2 electrons with g-C_3N_4 holes leads to the accumulation of holes and a lengthening of their lifespan in TiO_2 VB. Then the accumulated holes react with H_2O molecules to yield hydroxyl radicals, which are the main ROS accountable for RhB degradation. The holes TiO_2 VB can also degrade MB into by-products.

3.2.5. RhB and MB co-dye photocatalytic degradation

To conceptualize the discharge of actual water pollutants, RhB and MB dye pollutants were mixed, and the photocatalytic degradation of the mixed system was conducted for TiO_2/g-C_3N_4 nanocomposite. The condition for mixed system degradation was as follows: 50 mg of TiO_2/g-C_3N_4 nanocomposite was mixed with a 100 mL solution containing 10 mg L^{-1} RhB and 10 mg L^{-1} MB (50 mL each). Other photocatalytic conditions were kept the same as the one for individual dye degradation. The results of mixed system degradation are given in Figure 11. As evident from Figure 11a, the maximum absorbance peaks of RhB and MB decrease with an increase in irradiation time. The degradation efficiency of the mixed-dye system was obtained to be 97% and 92% for RhB and MB after 240 min of solar light irradiation, respectively (Figure 11b). The nanocomposite photocatalytic activity was more selective to RhB than MB, even though the adsorption favors MB over RhB. This can be ascribed to the difference in molecular weight. Additionally, although the irradiation time increases for mixed dye systems, the nanocomposite can still be considered an outstanding photocatalyst for insinuation in real applications.

Table 3. The distinction between the current study and previous studies on the synthesis of TiO_2/g-C_3N_4 photocatalyst for the photodegradation of organic dyes.

Synthetic method	Pollutants, Concentration	Degradation efficiency (%)	Irradiation time, Light source	Refs
Solvothermal (180 °C, 6 h)[a]	MB 10 mg L^{-1}	97.6	240 min 350 W Xenon lamp	[6]
Hydrothermal (180 °C, 4 h) – Calcination (500 °C, 2 h)[b]	RhB by 1 × 10^{-5} M	95.2	80 min Visible light	[55]
Hydrothermal (130 °C, 24 h) – Calcination (500 °C, 2 h)[c]	RhB 10 mg L^{-1}	99.9	60 min 500 W Xenon lamp	[54]
Pyrolysis (550 °C, 2 h)[d]	RhB 10 mg L^{-1}	97	40 min 300 W Xenon lamp	[56]
Hydrothermal process (180 °C, 12 h)[e]	RhB 20 mg L^{-1}	45	12 h, 5 W LED	[57]
Atomic layer deposition – Calcination (500 °C, 1 h)[f]	MO 4 mg L^{-1}	98.2	90 min 300 W Xenon lamp	[58]
Calcination method (350 °C, 5 h)[g]	RhB 10 mg L^{-1}	96	120 min 300 W Xenon lamp	Present work
	MB 10 mg L^{-1}	95	150 min 300 W Xenon lamp	
Calcination method (350 °C, 5 h)[g]	RhB + MB	>90%	240 min 300 W Xenon lamp	Present work

[a] Require higher pressure reactor, longer synthetic time, and utilize many chemical precursors.
[b] Higher temperature, long synthesis time, and some ice bath.
[c] Higher temperature and long synthesis time.
[d] Require higher temperature.
[e] Higher temperature required, long synthesis time, and utilize many precursors.
[f] Higher temperature, longer synthesis time, ice bath, and utilize many chemical precursors.
[g] Low-temperature synthesis route utilizing Guava leaf extracts as TiO_2 reductor.

The comparison of the current study with several previous literature reports is shown in Table 3. It can be noted that even though the reported literature shows relatively higher photodegradation efficiency in a shorter time, the synthetic methods used are time-consuming and require higher temperature, whereas the present work showed similar efficiency in a reasonable time, and the synthetic method utilizes low temperature with less chemical precursors used.

4. Conclusion

In this study, the degradation of RhB and MB on a formed direct S-scheme TiO_2/g-C_3N_4 heterojunction nanocomposite from simultaneous calcination of the TiO_2 precursors and pristine g-C_3N_4 was presented. The S-Scheme TiO_2/g-C_3N_4 nanocomposite demonstrates higher photocatalytic performance with high degradation efficiency for RhB (96%) and MB (92%) attained in 120 and 150 min of simulated solar light irradiation, respectively. The enhancement in photocatalytic performance of nanocomposite was accredited to the construction of the S-scheme heterojunction structure between TiO_2 and g-C_3N_4 which promote the enhancement of charge separation. The apparent reaction rate constant of the nanocomposite was 3.7 and 4.1 folds higher than TiO_2 and g-C_3N_4 for RhB degradation, and 2.5 and 4.1 folds higher than TiO_2 and g-C_3N_4, for MB degradation, respectively. The degradation efficiencies of RhB and MB remain above 85% after 4 degradation cycles. The trapping agent inhibition results illustrated that $OH^{\bullet}$ and $O_2^{\bullet -}$ radicals are dominant ROS responsible for the photodegradation of RhB, while h^+ and $O_2^{\bullet -}$ radicals are dominant in the photodegradation of MB. The nanocomposite also shows remarkable photocatalytic degradation efficiency in the degradation of mixed dye pollutants with more than 90% degradation efficiencies achieved in 240 min for both dyes under simulated solar light irradiation, indicating that the nanocomposite could be employed in real wastewater treatment. This study simply explored a novel approach for constructing a high-efficiency S-scheme heterojunction photocatalyst for water purification under solar light irradiation.

Declarations

Author contribution statement

Ntakadzeni Madima: Conceived and designed the experiments; Performed the experiments; Analyzed and interpreted the data; Wrote the paper.

Kebede K. Kefeni: Analyzed and interpreted the data; Contributed reagents, materials, analysis tools, or data.

Shivani B. Mishra: Conceived and designed the experiments; Contributed reagents, materials, analysis tools, or data.

Ajay K. Mishra: Conceived and designed the experiments; Analyzed and interpreted the data; Contributed reagents, materials, analysis tools, or data.

Funding statement

This work was supported by the Institute for Nanotechnology and Water Sustainability (iNanoWS) of the University of South Africa and the National Research Foundation (NRF), South Africa.

Data availability statement

The data that has been used is confidential.

Declaration of interests statement

The authors declare no conflict of interest.

Additional information

No additional information is available for this paper.

References

[1] N. Madima, S.B. Mishra, I. Inamuddin, A.K. Mishra, Carbon-based nanomaterials for remediation of organic and inorganic pollutants from wastewater. A review, Environ. Chem. Lett. 18 (2020) 1169–1191.

[2] A.N. Kulkarni, A.D. Watharkar, N.R. Rane, B.H. Jeon, S.P. Govindwar, Decolorization and detoxification of dye mixture and textile effluent by lichen Dermatocarpon vellereceum in fixed bed upflow bioreactor with subsequent oxidative stress study, Ecotoxicol. Environ. Saf. 148 (2018) 17–25.

[3] D. Rawat, R.S. Sharma, S. Karmakar, L.S. Arora, V. Mishra, Ecotoxic potential of a presumably non-toxic azo dye, Ecotoxicol. Environ. Saf. 148 (2018) 528–537.

[4] Y. Chen, L. Feng, H. Li, Y. Wang, G. Chen, Q. Zhang, Biodegradation and detoxification of Direct Black G textile dye by a newly isolated thermophilic microflora, Bioresour. Technol. 250 (2018) 650–657.

[5] P.T. Lum, K.Y. Foo, N.A. Zakaria, P. Palaniandy, Ash based nanocomposites for photocatalytic degradation of textile dye pollutants: a review, Mater. Chem. Phys. 241 (2020), 122405.

[6] X. Guo, J. Duan, C. Li, Z. Zhang, W. Wang, Fabrication of g-C_3N_4/TiO_2 photocatalysts with a special bilayer structure for visible light photocatalytic application, Colloids Surf. A Physicochem. Eng. Asp. 599 (2020), 124931.

[7] B. Zhang, X. He, X. Ma, Q. Chen, G. Liu, Y. Zhou, D. Ma, C. Cui, J. Ma, Y. Xin, In situ synthesis of ultrafine TiO_2 nanoparticles modified g-C_3N_4 heterojunction photocatalyst with enhanced photocatalytic activity, Separ. Purif. Technol. (2020) 247.

[8] P. Gündoğmuş, J. Park, A. Öztürk, Preparation and photocatalytic activity of g-C_3N_4/TiO_2 heterojunctions under solar light illumination, Ceram. Int. 46 (2020) 21431–21438.

[9] H. Wang, H. Li, Z. Chen, J. Li, X. Li, P. Huo, Q. Wang, TiO_2 modified g-C_3N_4 with enhanced photocatalytic CO_2 reduction performance, Solid State Sci. 100 (2020), 106099.

[10] D. Monga, S. Basu, Enhanced photocatalytic degradation of industrial dye by g-C_3N_4/TiO_2 nanocomposite: role of shape of TiO_2, Adv. Powder Technol. 30 (2019) 1089–1098.

[11] C. Wang, L. Hu, B. Chai, J. Yan, J. Li, Enhanced photocatalytic activity of electrospun nanofibrous TiO_2/g-C_3N_4 heterojunction photocatalyst under simulated solar light, Appl. Surf. Sci. 430 (2018) 243–252.

[12] V. Likodimos, Photonic crystal-assisted visible light activated TiO_2 photocatalysis, Appli. Catal. B: Environ. 230 (2018) 269–303.

[13] L. Zhou, L. Wang, J. Zhang, J. Lei, Y. Liu, The preparation, and applications of g-C_3N_4/TiO_2 heterojunction catalysts—a review, Res. Chem. Intermed. 43 (2017) 2081–2101.

[14] A. Shabani, G. Nabiyouni, J. Saffari, D. Ghanbari, Photo-catalyst Fe_3O_4/TiO_2 nanocomposites: green synthesis and investigation of magnetic nanoparticles coated on cotton, J. Mater. Sci. Mater. Electron. 27 (2016) 8661–8669.

[15] W. Ye, Y. Shao, X. Hu, C. Liu, C. Sun, Highly enhanced photoreductive degradation of polybromodiphenyl ethers with g-C_3N_4/TiO_2 under visible light irradiation, Nanomaterials 7 (2017) 2–11.

[16] M.A. Alcudia-Ramos, M.O. Fuentez-Torres, F. Ortiz-Chi, C.G. Espinosa-González, N. Hernández-Como, D.S. García-Zaleta, M.K. Kesarla, J.G. Torres-Torres, V. Collins-Martínez, S. Godavarthi, Fabrication of g-C_3N_4/TiO_2 heterojunction composite for enhanced photocatalytic hydrogen production, Ceram. Int. 46 (2020) 38–45.

[17] H. Wei, W.A. Mcmaster, J.Z.Y. Tan, L. Cao, D. Chen, R.A. Caruso, Mesoporous TiO_2/g-C_3N_4 microspheres with enhanced visible-light photocatalytic activity, J. Phys. Chem. 121 (2017) 22114–22122.

[18] A. Raza, H. Shen, A.A. Haidry, S. Cui, Hydrothermal synthesis of Fe_3O_4/TiO_2/g-C_3N_4: advanced photocatalytic application, Appl. Surf. Sci. 488 (2019) 887–895.

[19] Y. Yu, W. Xu, J. Fang, D. Chen, T. Pan, W. Feng, Y. Liang, Z. Fang, Soft-template assisted construction of superstructure TiO_2/SiO_2/g-C_3N_4 hybrid as efficient visible-light photocatalysts to degrade berberine in seawater via an adsorption-photocatalysis synergy and mechanism insight, Appl. Catal. B: Environ. 268 (2020), 118751.

[20] Y. Zhou, M. Yu, H. Liang, J. Chen, L. Xu, J. Niu, Novel dual-effective Z-scheme heterojunction with g-C_3N_4, Ti_3C_2 MXene and black phosphorus for improving visible light-induced degradation of ciprofloxacin, Appl. Catal. B: Environ. 291 (2021), 120105.

[21] C. Feng, L. Tang, Y. Deng, J. Wang, Y. Liu, X. Ouyang, H. Yang, J. Yu, J. Wang, A novel sulfur-assisted annealing method of g-C_3N_4 nanosheet compensates for the loss of light absorption with further promoted charge transfer for photocatalytic production of H_2 and H_2O_2, Appl. Catal. B: Environ. 281 (2021), 119539.

[22] C. Wang, W. Zhu, Y. Xu, H. Xu, M. Zhang, Y. Chao, S. Yin, H. Li, J. Wang, Preparation of TiO_2/g-C_3N_4 composites and their application in photocatalytic oxidative desulfurization, Ceram. Int. 40 (2014) 11627–11635.

[23] H. Zhu, X. Yang, M. Zhang, Q. Li, J. Yang, Construction of 2D/2D TiO_2/g-C_3N_4 nanosheet heterostructures with improved photocatalytic activity, Mater. Res. Bull. 125 (2020), 110765.

[24] R.A. Senthil, J. Theerthagiri, A. Selvi, J. Madhavan, Synthesis and characterization of low-cost g-C_3N_4/TiO_2 composite with enhanced photocatalytic performance under visible-light irradiation, Opt. Mater. 64 (2017) 533–539.

[25] R. Acharya, K. Parida, A review on TiO_2/g-C_3N_4 visible-light-responsive photocatalysts for sustainable energy generation and environmental remediation, J. Environ. Chem. Eng. 8 (2020), 103896.

[26] G. Xiao, S. Xu, P. Li, H. Su, Visible-light-driven activity and synergistic mechanism of TiO_2@g-C_3N_4 heterostructured photocatalysts fabricated through a facile and green procedure for various toxic pollutants removal, Nanotechnology 29 (2018).

[27] Y. Tan, Z. Shu, J. Zhou, T. Li, W. Wang, Z. Zhao, One-step synthesis of nanostructured g-C_3N_4/TiO_2 composite for highly enhanced visible-light photocatalytic H_2 evolution, Appl. Catal. B: Environ. 230 (2018) 260–268.

[28] R. Hao, G. Wang, H. Tang, L. Sun, C. Xu, D. Han, Template-free preparation of macro/mesoporous g-C_3N_4/TiO_2 heterojunction photocatalysts with enhanced visible light photocatalytic activity, Appl. Catal. B: Environ. 187 (2016) 47–58.

[29] G. Kandregula, K.V. Rao, S. Chidurala, Synthesis of TIO_2 nanoparticles from orange fruit waste from orange fruit waste centre for nano science and technology , Institute of science and technology introduction: nanoscience & technology have the ability to see and to control, Int. J. Multidiscipl. Ad. Res. Trends II (I) (2015) 82–90.

[30] M. Sundrarajan, S. Gowri, Green synthesis of titanium dioxide nanoparticles by nyctanthes arbor-tristis leaves extract, Chalcogenide Lett. 8 (2011) 447–451.

[31] N. Roy, Y. Park, Y. Sohn, K.T. Leung, D. Pradhan, Green synthesis of anatase TiO_2 nanocrystals with diverse shapes and their exposed facets-dependent photoredox activity, ACS Appl. Mater. Interfaces 6 (2014) 16498–16507.

[32] T. Santhoshkumar, A.A. Rahuman, C. Jayaseelan, G. Rajakumar, S. Marimuthu, A.V. Kirthi, K. Velayutham, J. Thomas, J. Venkatesan, S.K. Kim, Green synthesis of titanium dioxide nanoparticles using Psidium guajava extract and its antibacterial and antioxidant properties, Asian Pac. J. Trop. Med. 7 (2014) 968–976.

[33] M. Kumar, A. Mehta, A. Mishra, J. Singh, M. Rawat, S. Basu, Biosynthesis of tin oxide nanoparticles using Psidium Guajava leave extract for photocatalytic dye degradation under sunlight, Mater. Lett. 215 (2018) 121–124.

[34] K. Thandapani, M. Kathiravan, E. Namasivayam, I.A. Padiksan, G. Natesan, M. Tiwari, B. Giovanni, V. Perumal, Enhanced larvicidal, antibacterial, and photocatalytic efficacy of TiO_2 nanohybrids green synthesized using the aqueous leaf extract of Parthenium hysterophorus, Environ. Sci. Pollut. Control Ser. 25 (2018) 10328–10339.

[35] N. Nazar, I. Bibi, S. Kamal, M. Iqbal, S. Nouren, K. Jilani, M. Umair, S. Ata, Cu nanoparticles synthesis using biological molecule of P. granatum seeds extract as reducing and capping agent: growth mechanism and photo-catalytic activity, Int. J. Biol. Macromol. 106 (2018) 1203–1210.

[36] I. Bibi, N. Nazar, M. Iqbal, S. Kamal, H. Nawaz, S. Nouren, Y. Safa, K. Jilani, M. Sultan, S. Ata, F. Rehman, M. Abbas, Green and eco-friendly synthesis of cobalt-oxide nanoparticle: characterization and photo-catalytic activity, Adv. Powder Technol. 28 (2017) 2035–2043.

[37] S.P. Goutam, G. Saxena, V. Singh, A.K. Yadav, R.N. Bharagava, K.B. Thapa, Green synthesis of TiO_2 nanoparticles using leaf extract of Jatropha curcas L. for photocatalytic degradation of tannery wastewater, Chem. Eng. J. 336 (2018) 386–396.

[38] N.S. Sampath Kumar, N.M. Sarbon, S.S. Rana, A.D. Chintagunta, S. Prathibha, S.K. Ingilala, S.P. Jeevan Kumar, B. Sai Anvesh, V.R. Dirisala, Extraction of bioactive compounds from Psidium guajava leaves and its utilization in preparation of jellies, Amb. Express 11 (2021).

[39] N.E. Sunny, S.S. Mathew, N. Chandel, P. Saravanan, R. Rajeshkannan, M. Rajasimman, Y. Vasseghian, N. Rajamohan, S.V. Kumar, Green synthesis of titanium dioxide nanoparticles using plant biomass and their applications-a review, Chemosphere 300 (2022), 134612.

[40] N. Madima, K.K. Kefeni, S.B. Mishra, A.K. Mishra, A.T. Kuvarega, Fabrication of magnetic recoverable Fe_3O_4/TiO_2 heterostructure for photocatalytic degradation of rhodamine B dye, Inorg. Chem. Commun. (2022).

[41] J. Wang, J. Huang, H. Xie, A. Qu, Synthesis of g-C_3N_4/TiO_2 with enhanced photocatalytic activity for H2 evolution by a simple method, Int. J. Hydrogen Energy 39 (2014) 6354–6363.

[42] J. Li, M. Zhang, Q. Li, J. Yang, Enhanced visible light activity on direct contact Z-scheme g-C_3N_4-TiO_2 photocatalyst, Appl. Surf. Sci. 391 (2017) 184–193.

[43] X. Du, X. Bai, L. Xu, L. Yang, P. Jin, Visible-light activation of persulfate by TiO_2/g-C_3N_4 photocatalyst toward efficient degradation of micropollutants, Chem. Eng. J. 384 (2020).

[44] A. Tripathi, S. Narayanan, Impact of TiO_2 and TiO_2/g-C_3N_4 nanocomposite to treat industrial wastewater, Environ. Nanotechnol. Monit. Manag. 10 (2018) 280–291.

[45] J. Lei, Y. Chen, L. Wang, Y. Liu, J. Zhang, Highly condensed g-C_3N_4-modified TiO_2 catalysts with enhanced photodegradation performance toward acid orange 7, J. Mater. Sci. 50 (2015) 3467–3476.

[46] B. Zhang, X. He, X. Ma, Q. Chen, G. Liu, Y. Zhou, D. Ma, C. Cui, J. Ma, Y. Xin, In situ synthesis of ultrafine TiO_2 nanoparticles modified g-C_3N_4 heterojunction photocatalyst with enhanced photocatalytic activity, Separ. Purif. Technol. (2020) 247.

[47] Y. Wu, D. Meng, Q. Guo, D. Gao, L. Wang, Study on TiO_2/g-C_3N_4 S-Scheme heterojunction photocatalyst for enhanced formaldehyde decomposition, Opt. Mater. 126 (2022), 112213.

[48] P.J. Mafa, M.E. Malefane, A.O. Idris, D. Liu, J. Gui, B.B. Mamba, A.T. Kuvarega, Multi-elemental doped g-C3N4 with enhanced visible light photocatalytic Activity: insight into naproxen Degradation, Kinetics, effect of Electrolytes, and mechanism, Separ. Purif. Technol. 282 (2022), 120089.

[49] Y. Sheng, Z. Wei, H. Miao, W. Yao, H. Li, Y. Zhu, Enhanced organic pollutant photodegradation via adsorption/photocatalysis synergy using a 3D g-C_3N_4/TiO_2 free-separation photocatalyst, Chem. Eng. J. 370 (2019) 287–294.

[50] Y. Zhang, X. Ren, L. Yang, Z. Chen, Z-scheme TiO_2/g-C_3N_4 composites prepared by hydrothermal assisted thermal polymerization with enhanced visible light photocatalytic activity, Res. Chem. Intermed. 47 (2021) 1503–1518.

[51] K.D. Arunachalam, Bio-adsorption of methylene blue dye using chitosan-extracted from Fenneropenaeus indicus shrimp shell waste, J. Aquacult. Mar. Biol. 10 (2021) 146–150.
[52] G. Singh, H.B. Dizaji, H. Puttuswamy, S. Sharma, Biogenic nanosilica synthesis employing agro-waste rice straw and its application study in photocatalytic degradation of cationic dye, Sustainability (2022) 14.
[53] A. Toghan, H.M. Abd El-Lateef, K.K. Taha, A. Modwi, Mesoporous TiO_2@g-C_3N_4 composite: construction, characterization, and boosting indigo carmine dye destruction, Diam. Relat. Mater. 118 (2021), 108491.
[54] M. Song, M. Li, Y. Guo, X. Huang, S. Wang, L. Ren, L. Li, Y. Wu, Facile fabrication of ordered assembled TiO_2/g-C_3N_4 nanosheets with enhanced photocatalytic activity, Ceram. Int. 47 (2021) 15594–15603.
[55] R. Hao, G. Wang, C. Jiang, H. Tang, Q. Xu, In situ hydrothermal synthesis of g-C_3N_4/TiO_2 heterojunction photocatalysts with high specific surface area for Rhodamine B degradation, Appl. Surf. Sci. 411 (2017) 400–410.
[56] S. Feng, F. Li, Photocatalytic dyes degradation on suspended and cement paste immobilized TiO_2/g-C_3N_4 under simulated solar light, J. Environ. Chem. Eng. 9 (2021), 105488.
[57] W. Tao, M. Wang, R. Ali, S. Nie, Q. Zeng, R. Yang, W.M. Lau, L. He, H. Tang, X. Jian, Multi-layered porous hierarchical TiO_2/g-C_3N_4 hybrid coating for enhanced visible light photocatalysis, Appl. Surf. Sci. 495 (2019), 143435.
[58] T.Q. Zi, X.R. Zhao, C. Liu, Y.Q. Cao, A.D. Li, A facile route to prepare TiO_2/g-C_3N_4 nanocomposite photocatalysts by atomic layer deposition, J. Alloys Compd. 855 (2021), 157446.